PAPER

Check for updates

Nanoconfinement effects of chemically reduced graphene oxide nanoribbons on poly(vinyl chloride)†

J. H. Choe,[a] J. Jeon,[a] M. E. Lee,[a] J. J. Wie, [ID] [a,b] H.-J. Jin [ID] *[a,b] and Y. S. Yun*[c]

Polymeric nanocomposites with graphene-based nanocarbons (GNCs) have been extensively studied with emphasis on the percolation of nanofillers toward electrical, rheological, and mechanical reinforcement. In this study, we report an unusual indirect reinforcing phenomenon of highly defective GNCs dispersed in the poly(vinyl chloride) (PVC) matrix *via* densification of the polymer packing originating from nanoscale confinement. Herein, chemically reduced graphene oxide nanoribbons (C-rGONRs) are employed as a nanofiller. The inclusion of defective and oxygen-functionalized C-rGONRs resulted in a dramatic densification of the PVC host with extremely low C-rGONR loading, largely exceeding the theoretical calculation from a rule of mixture. Along with the densification, the glass transition temperature of PVC also increased by 28.6 °C at 0.1 wt% filler loading. Remarkably, the oxygen barrier property and mechanical toughness under tension for the PVC/C-rGONR nanocomposite were the maximum when the greatest densification occurred. The structure−property relationship of the nanocomposites has been discussed with an emphasis on the nanoscale confinement phenomenon.

Introduction

Over the last century, polymers have attracted great attention as suitable candidates outperforming metals and inorganic materials in some conventional industrial fields owing to their facile processability, mass productivity, and competitive cost.[1,2] In addition, the kaleidoscopic physical properties of polymers dependent on the chain configuration, degree of crystallization, molecular weight, polydispersity index, and viscoelasticity make them versatile for various applications.[3–5] The physical properties of polymers can be further improved with the introduction of carbon-based nanofillers (CNFs). Accordingly, polymer nanocomposites based on such CNFs possessing good physical properties have been studied extensively.[6–13] The reinforcing effects of CNFs can be classified as two different mechanisms. The first effect originates from a significant property gap between the polymer matrix and CNFs; the outstanding physical properties of CNFs can

intensify the original properties of the polymer matrix and/or endow a new function.[14–17] For example, graphene shows a high Young's modulus (~1.0 TPa),[7] high electrical conductivity (~106 S cm⁻¹),[18] and exceptional thermal conductivity (~5000 W m⁻¹ K⁻¹),[19] which can enable the polymer matrix to withstand intensive stress and heat distortion. Moreover, graphene can increase the diffusion length of gas molecules in polymer matrices, providing them a barrier property applicable in advanced technological fields, *e.g.*, in flexible organic displays and bio-electronics.[20,21] The other is an indirect reinforcing effect of CNFs, affecting the crystallinity and/or interchain conformation of polymers. Not only can the edge sites of poly-hexagonal carbon structures be a nucleation site for crystallites of polymer chains but amorphous polymer chains can also be rearranged on the surface of their basal plane, resulting in a change in the intrinsic properties of the polymer matrix.[22–25] Considering that the physical properties of the most practically used CNFs do not reach their theoretical properties due to the presence of numerous defects, a considerable fraction of their reinforcing effects could be induced by nanoconfinement effects affecting the intrinsic properties of the polymer matrix. However, most reported studies focused on the property gap between CNFs and the polymer matrix, although CNFs have a large number of topological defects.[26]

Graphene nanoribbons (GNRs) constitute a family of sp² carbon allotropes consisting of an infinite quasi-one-dimensional hexagonal carbon array with a high aspect ratio of >100,

[a]Department of Polymer Science and Engineering, Inha University, Incheon 22212, South Korea. E-mail: hjjin@inha.ac.kr
[b]World Class Smart Laboratory (WCSL), Inha University, Incheon 22212, South Korea
[c]Department of Chemical Engineering, Kangwon National University, Samcheok 245-711, South Korea. E-mail: ysyun@kangwon.ac.kr
†Electronic supplementary information (ESI) available. See DOI: 10.1039/c7nr07098e

which have large interfacial areas and edge sites[27,28] and exhibit outstanding thermomechanical properties (modulus: ~1 TPa; thermal conductivity: ~2400 W m^{-1} K^{-1}).[29,30] Owing to the high aspect ratio of GNRs, a percolation threshold can be achieved at a low filler content and polymer chains can be highly affected by the large number of active sites. Additionally, when GNRs are prepared by the unzipping of carbon nanotubes (CNTs), multitudinous oxygen functional groups[27] and topological defects are introduced on their surface, a considerable number of which remain even after chemical reduction.[31,32] The extensive defect sites can maximize the interaction between the polymer matrix and the unzipped graphene oxide nanoribbons (GONRs),[23,33,34] while the intrinsic physical properties of GONRs deteriorate.[7,35] Hence, the reinforcing behaviors of GONRs could differ from those of perfect GNRs and induce inferior reinforcing effects owing to the property gap but result in a more critical change in the polymer properties.

In this study, GONRs were prepared by unzipping CNTs and reduced with hydrazine in order to confirm the reinforcing effects of chemically reduced GONRs (C-rGONRs) in the polymer matrix.[7,36] In order to maximize the interaction between the polymer and C-rGONRs, a polar polymer matrix poly(vinyl chloride) (PVC) was selected. The C-rGONRs have defective hexagonal carbon structures with a few-nanometer-scale crystal domains and a large number of oxygen functional groups (C/O ratio of 6.3), which led to a homogeneous dispersion of the C-rGONRs in the polar PVC matrix. It is noteworthy that the density of the PVC matrix increased dramatically from 1.409 to 1.441 g cm^{-3} on the addition of 0.1 wt% of C-rGONRs.[37] Considering a C-rGONR density of 1.652 g cm^{-3}, a density increase of ~0.032 g cm^{-3} is exceptionally high. This unusual densification in the PVC/C-rGONR nanocomposite implies a large perturbation in the polymer segmental conformation through strong nanoscale interactions between the

PVC and C-rGONRs. We found that the oxygen transmission rates of PVC and PVC/C-rGONR nanocomposites are closely connected with the density of the matrix. Moreover, a dramatic improvement of ~41% in the toughness was achieved for the PVC/C-rGONR nanocomposites along with the densification. These results reveal a remarkable nanoconfinement effect originating from the C-rGONRs with a defective carbon structure in the polymer matrix.

Results and discussion

Multi-walled carbon nanotubes (MWCNTs) with a high aspect ratio (>100) and high persistence length (l_{sp} ~ 520 nm) were unzipped in the axial direction (Fig. S1†), resulting in GONRs with a high contour length of several micrometers, as shown in Fig. 1(a) and (b).[38,39] High-resolution field-emission transmission electron microscopy (FE-TEM) images demonstrated that the GONRs had a rough surface and an amorphous carbon structure with no long-range carbon ordering (Fig. 1(c) and (d)). In addition, the GONR particles were composed of a few graphene-based layers with a thickness below several nanometers (Fig. 1(d)). After chemical reduction with hydrazine, there was no significant change in their morphologies and microstructures (Fig. 1(e)–(h)). Microstructures of the GONRs and C-rGONRs were further characterized by X-ray diffraction (XRD) and Raman spectroscopy (Fig. 2). The XRD patterns of both samples were similar to each other and showed a very broad graphite (002) peak, indicating poor graphitic stacking ordering (Fig. 2(a)). In the Raman spectra of both samples, distinct D and G bands were observed, corresponding to the disorder in the A$_{1g}$ breathing mode of the six-membered aromatic ring near the basal edge and reflecting the hexagonal structure related to the E$_{2g}$ vibration mode of the sp^2-hybridized carbon atoms, respectively (Fig. 2(b)). Therefore, the presence of D
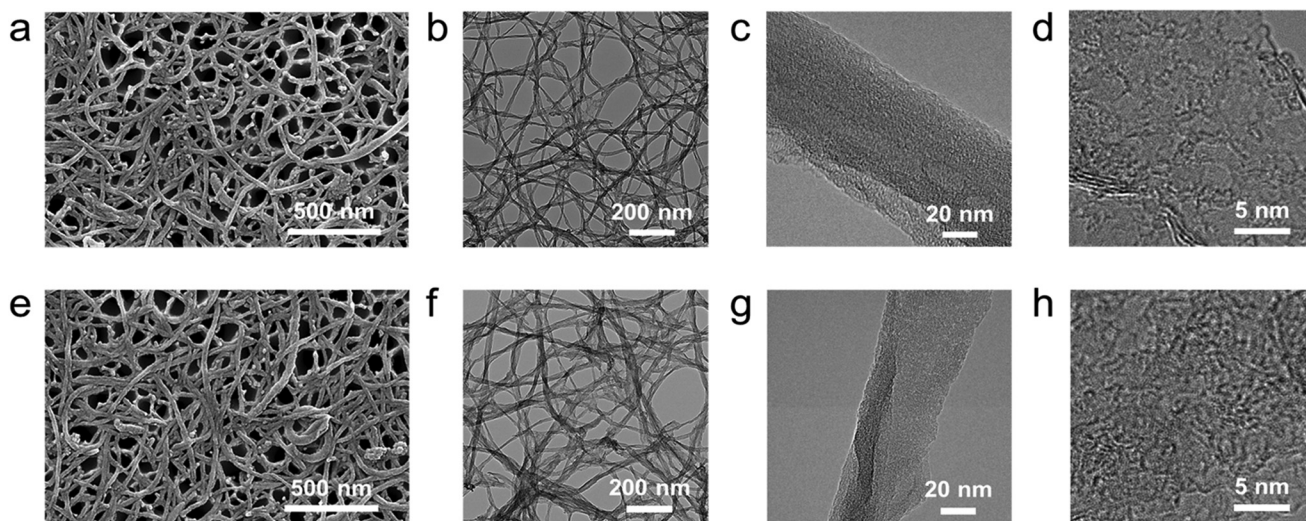

Fig. 1 FE-SEM micrographs of (a) GONRs and (e) C-rGONRs. FE-TEM micrographs of (b), (c) GONRs and (f), (g) C-rGONRs at different magnifications, and high-resolution FE-TEM images of (d) GONRs and (h) C-rGONRs.
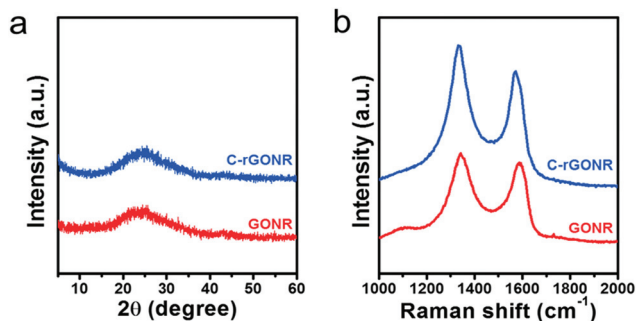
Fig. 2 (a) XRD patterns and (b) Raman spectra of GONRs and C-rGONRs.

and G bands indicates that the GONRs and C-rGONRs are composed of poly-hexagonal carbon structures. The D to G band intensity ratio (I_D/I_G) represents the size of the ordered poly-hexagonal carbon structures. As the characteristic peaks of the D and G bands were fused, approximate I_D/I_G ratios of GONRs and C-rGONRs were utilized to estimate a specific crystalline domain size from the deconvoluted Raman spectra, which was 1.24 for both samples. And their domain sizes were calculated to be 13.4 nm.[40] Hence, from the Raman results, we could confirm that GONRs and C-rGONRs are composed of defective hexagonal carbon structures with nanometer-scale crystal domains.

The surface properties of GONRs and C-rGONRs were investigated by X-ray photoelectron spectroscopy (XPS), as shown in Fig. 3. The C 1s spectra of GONRs indicate diverse carbon bonding configurations such as C=C, C–C, C–O, and C=O bonding centered at 284.4, 285.0, 286.5, and 288.5 eV, respectively (Fig. 3(a)). After chemical reduction, similar characteristic peaks were found while the intensities for the relative C–O and C=O bonding peaks decreased significantly and those for the C=C and C–C bonding structures increased (Fig. 3(b)). In the O 1s spectra of GONRs, the C=O and C–O bonding peaks were found to be centered at 531.9 and 532.9 eV, respectively
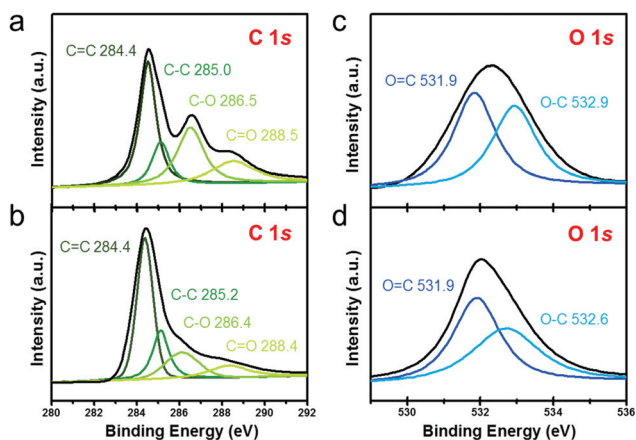
(Fig. 3(c)), and the relative intensity of the C=O to C–O bonding peaks increased slightly after chemical reduction (Fig. 3(d)). The C/O ratio for GONRs was 2.3, which increased remarkably to 6.3 after chemical reduction. However, it is noteworthy that a considerable number of oxygen functional groups remained in C-rGONRs. The polar surface properties of C-rGONRs are key to achieving homogeneous dispersion in dimethylformamide (DMF), which is indispensable for achieving the nanocomposite.[41] In a dispersion stability test, C-rGONRs showed a highly stable dispersion behavior during 24 h, which outperformed the GONRs (Fig. S3†). A stable colloidal dispersion suggests that the mixing energy (ΔG_{mix}) between GONRs and DMF has a negative value. Considering that the entropy value of ΔG_{mix} calculated using Flory's equation is small, ΔH_{mix} could be an extremely small or negative value according to the equation $\Delta H_{mix} < T\Delta S_{mix}$. According to eqn (1), the enthalpy of ΔG_{mix} depends on the balance between GONRs and the solvent surface energy. Therefore, the dispersion result confirmed that C-rGONRs have more comparable surface energy with DMF. Considering that DMF is a good solvent for PVC, it is expected that C-rGONRs have favorable interfacial adhesion with the PVC matrix:

$$\frac{\Delta H_{mix}}{V_{mix}} \approx \frac{2}{T_G}(\delta_G - \delta_{sol})^2\phi \qquad (1)$$

Further direct evidence of the compatibility between PVC and C-rGONRs was obtained from contact angle measurements. As shown in Fig. S4,† PVC and C-rGONR films showed similar contact angles with a water or glycerol droplet, while GONRs showed a much lower value. The specific surface energies calculated from the contact angle results are summarized in Table S1.† Fig. 4 shows the fractured surface images of neat PVC and PVC/C-rGONR nanocomposites at 0.1 wt% C-rGONR loading. Unlike the smooth surface of the neat PVC, homogeneously dispersed nanofillers resulted in a rough surface of the nanocomposites where strong polymer–filler interactions could be established at the nanoscale.[13]

For the polymer nanocomposites, the dimension of nanoparticles was comparable to the Kuhn length and was smaller
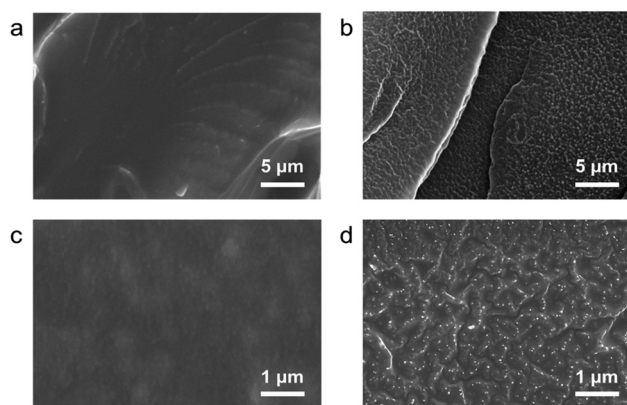

Fig. 3 XPS C 1s spectra of (a) GONRs and (b) C-rGONRs; O 1s spectra of (c) GONRs and (d) C-rGONRs.

Fig. 4 FE-SEM images for a fractured surface of (a), (c) neat PVC and (b), (d) PVC/0.1 wt% C-rGONR nanocomposites.

than the radius of gyration of the polymers. Hence, the isotropic random coil conformation of the polymer segment can be perturbed by the presence of nanoparticles. Based on these geometric constraints, various computational studies predicted the perturbation of molecular packing of the polymer matrices. For example, de Pablo and his colleagues reported the entropy-driven evolution of polymer anisotropy at the polymer–nanoparticle interfaces *via* Monte Carlo simulations.[42] Tuteja *et al.* reported the expansion of the polymer dimensions by a small angle neutron scattering (SANS) technique in thermal polymer nanocomposites where crosslinked polystyrene (PS) nanoparticles were dispersed in PS matrices.[43] Molecular dynamics simulation also predicted the generation of density fluctuation near nanoparticles by the inclusion of nanoparticles.[44]

The nanoconfinement effect on the density of PVC nanocomposites was pronounced and is summarized in Fig. 5(a). The neat PVC density of 1.409 g cm^{-3} increased to 1.411, 1.420, 1.438, 1.441, and 1.433 g cm^{-3} on the addition of C-rGONRs at 0.01, 0.03, 0.05, 0.1, and 0.2 wt% concentration, respectively. As C-rGONRs have a density of 1.652 g cm^{-3}, this dramatic densification cannot be explained by a simple rule of mixture. Hence, perturbation of the polymer packing near nanofillers *via* nanoconfinement could be responsible for the density change that led to a reduction in the free volume of the nanocomposites.[37,45] The Kuhn length of PVC is 2.6 nm and the radius of gyration of PVC is expected to be 8–9 nm considering the molecular weight.[46] Here, half of the nanofiller thickness was ~2–3 nm, which is comparable to the PVC Kuhn length and smaller than the PVC radius of gyration. Hence, the chain conformation and packing of the PVC segment could be distorted by the C-rGONR nanofillers, resulting in the high-density region in comparison with those of the

bulk polymer matrices. In addition to entropic contributions, high polarizability of the bulky chlorine side chain in PVC could induce strong molecular interactions by forming multitudinous secondary bonding.[47] The PVC/C-rGONR nanocomposites could form strong hydrogen and halogen bonding with PVC since the C-rGONRs homogeneously dispersed in the PVC matrix had a high interfacial area and a large number of oxygen and hydrogen atoms on their surface.[48,49] The interaction was confirmed *via* infrared (IR) spectroscopy and XPS characterization (Fig. S5†). As shown in Fig. S5(a),† the main O–H bonding peak of C-rGONRs – centered at ~3435 cm^{-1} – was red-shifted after the addition of the C-rGONRs to the PVC host. Accordingly, the main O–H bonding peak of PVC/C-rGONRs was found at ~3298 cm^{-1}. Considering that the PVC chains show no O–H bonding peaks, the red-shifted peak could originate from the C-rGONRs added to the PVC host. The red-shifted peak suggests that the strong interaction between O–H groups and PVC chains induced the extension of the oxygen–hydrogen bonding distance, resulting in a decrease of the wavenumber of O–H bonding. Moreover, in the XPS Cl 2p spectra (Fig. S5(b and c)†), the main C–Cl bonding of neat PVC chains – centered at 200.4 eV – was red-shifted to 200.0 eV by the addition of C-rGONRs. The result also supports the presence of halogen bonding in the PVC/C-rGONR nanocomposite.

Another point to note is the non-linear increase in the density with the loading content of C-rGONRs. If C-rGONRs were randomly dispersed in the polymer host without agglomerations, the density should change linearly as a function of the C-rGONR concentration. However, the maximum density was achieved at 0.1 wt% loading, implying that a filler loading too high obstructs the reinforcing behaviors of the C-rGONRs. As the filler concentration increases, nanoparticles can aggregate through enhanced filler–filler interactions that can cause further reduction in interparticle separation. The modification of the intrinsic properties of the PVC matrix with C-rGONRs was also confirmed by the oxygen transmission barrier performances. According to the Cussler-random array model, as shown in eqn (2), it is expected that a ribbon-type filler with a high aspect ratio of >100 typically leads to a reduction in the oxygen transmission rate by approximately 5% owing to tortuous effects:[50]

$$R_{p} = \frac{1-\phi}{(1+\alpha\phi/3)^2}\phi \quad (2)$$

where R_p is the relative permeability (= ratio of oxygen transmission rate (OTR), P/P_0); P is the permeability coefficient of the PVC nanocomposite [cc mm m^{-2} day^{-1} atm^{-1}]; P_0 is the permeability coefficient of the neat PVC [cc mm m^{-2} day^{-1} atm^{-1}]; α is the aspect ratio of C-rGONRs; and ϕ is the volume fraction of C-rGONRs in the PVC matrix. However, as shown in Fig. 5(a), the PVC nanocomposites including 0.1 wt% C-rGONRs showed an OTR reduction of approximately 54% compared with that of neat PVC. This remarkable result strongly supports that the nanoconfinement effects of
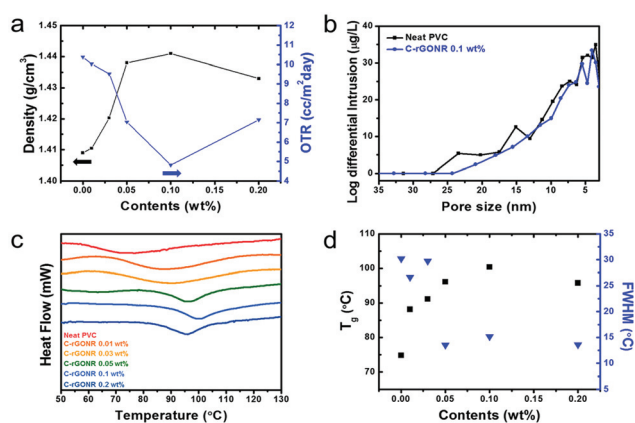
Fig. 5 (a) Density and oxygen transmission rate curves for PVC/C-rGONR nanocomposites at various loading contents of C-rGONRs. (b) Distribution of pores in neat PVC and 0.1 wt% C-rGONR nanocomposite according to Hg porosimetry. (c) DSC thermograms of neat PVC and PVC/C-rGONR nanocomposites at various filler concentrations. (d) Summarized glass transition temperature and full width at half maximum of neat PVC and PVC/C-rGONR nanocomposites against C-rGONR contents.

C-rGONRs strongly affected the OTR reduction of the PVC nanocomposites. To further confirm the densified polymer packing and reduced free volume, Hg-porosimetry was conducted at different pressures. As shown in Fig. 5(b), neat PVC had nanopores of up to 27 nm pore size. The addition of 0.1 wt% C-rGONRs induced the obvious suppression of large pores that can support the aforementioned OTR results. As a result, the total porosity of 2.82% for the neat PVC decreased to 2.51% for the 0.1 wt% C-rGONR nanocomposite.

The inclusion of nanoparticles is known to manipulate the glass transition behaviors of polymer composites.[51,52] As shown in Fig. 5(c), the differential scanning calorimetry (DSC) thermograms of the PVC nanocomposites indicated a significant free volume reduction as evident from a dramatic increase (∼28.6 °C) in the glass transition temperature (T_g) on inclusion of C-rGONRs. The summarized DSC results are shown in Fig. 5(d). In addition to the T_g changes, the full width at half maximum (FWHM) decreased, demonstrating that the relaxation mode of the polymer became more uniform by nanoconfinement. Interestingly, the tendency of T_g and FWHM coincided with the densification behaviors and OTR properties of the nanocomposites. Moreover, further direct evidence was obtained using FE-TEM micrographs which were characterized after preparing a thin film of ∼100 nm thickness through the ultra-microtoming of the PVC/C-rGONR nanocomposite, as shown in Fig. 7. The images show C-rGONR particles in the PVC matrix, where the interface between the C-rGONRs and PVC host shows little bit more contrast, indicating a higher electronic density. The high contrast region ranges for several nanometers with C-rGONRs as the center, which supports the dense packing of PVC chains in the vicinity of C-rGONRs. Based on the structure–property relationship of the nanocomposites from the density, OTR, porosity, and DSC characterization, a schematic image describing the modified polymer packing by nanoconfinement effects of C-rGONRs is presented in Fig. 6.

In order to observe the reinforcing effects of C-rGONRs in the PVC matrix, the mechanical properties of neat PVC and
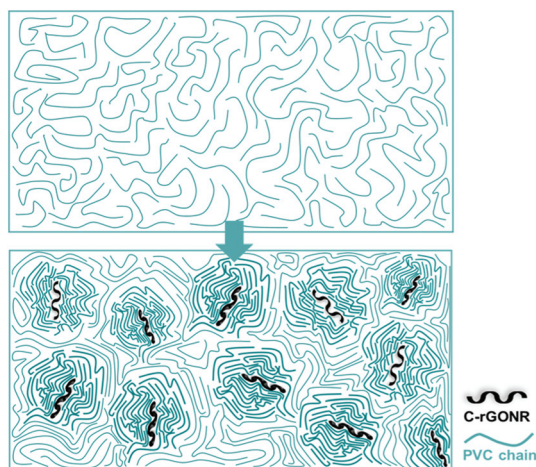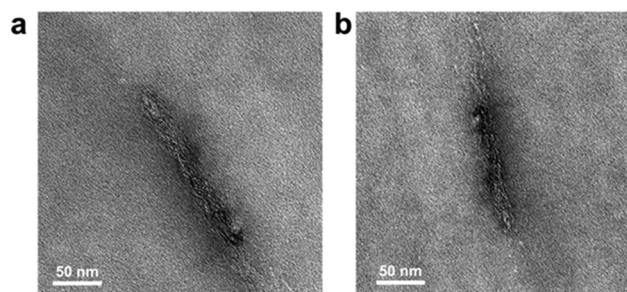

Fig. 7 (a, b) FE-TEM photographs of C-rGONRs dispersed in the PVC matrix.
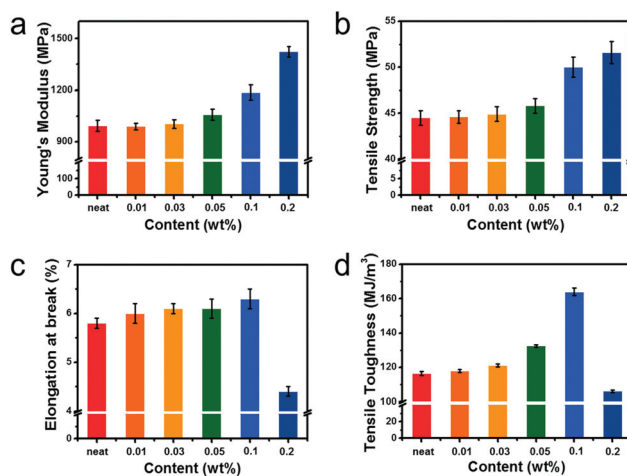

Fig. 8 Mechanical properties of PVC/C-rGONR nanocomposites; bar graphs of (a) Young's modulus, (b) tensile strength, (c) elongation at break, and (d) tensile toughness.

PVC/C-rGONR nanocomposites were investigated by ultimate testing machine (UTM) tests (Fig. 8). The Young's modulus of 993.8 MPa for neat PVC gradually increased as the C-rGONR loading increased. At 0.1 and 0.2 wt% loadings of C-rGONRs, the Young's modulus values of 1186.8 and 1423.4 MPa were achieved, respectively, which denoted 19 and 43% reinforcement in comparison with the neat PVC. In addition, the tensile strength of 44.5 MPa for neat PVC also continuously increased on the addition of more C-rGONRs and reached 50.0 and 51.6 MPa for the PVC matrices including 0.1 and 0.2 wt% C-rGONRs, respectively, which corresponded to 12 and 16% enhancement, compared to that of the neat PVC. Although remarkable enhancements of the tensile strength on PVC hosts have been reported, when graphene-based reinforcement was added, the PVC/C-rGONR nanocomposites show the highest tensile strength with a significantly low filler loading in the reported results.[53–56] The C-rGONRs were homogeneously dispersed in the PVC matrix and showed good interfacial adhesion with PVC. Therefore, efficient load transfer from relatively ductile PVC molecules to the stiff filler could be possible. Hence, improvement of the Young's modulus and tensile strength could be induced by the property gap between

Fig. 6 Schematic exhibiting densification of the PVC matrix via nanoconfinement effects by addition of C-rGONRs.

C-rGONRs and the PVC matrix. On the other hand, an insignificant increase in elongational properties was observed at ~0.1 wt% of C-rGONR loading, followed by a rapid decrease at 0.2 wt% filler loading. The increased mechanical stiffness of a conventional polymer composite typically occurs at the expense of reduced elongational properties, resulting in an insignificant increase in toughness (or energy to break). However, in this study, the PVC/C-rGONR nanocomposite demonstrated a simultaneous increase in the modulus, strength, and strain-to-failure by the inclusion of the nanofiller which is a unique property of nanocomposites. This toughness enhancement suggests that the C-rGONRs effectively behaved as load transfer sites and prohibited crack propagation. The largest toughness reinforcement was measured for the PVC/ 0.1 wt% C-rGONR nanocomposite (164.0 MJ m^{-3}, 41% reinforcement). This composition corresponded to the largest densification where the largest nanoconfinement is expected. As higher filler loading reduces the interparticle separation distance that can increase the filler–filler interactions, the nanoscale interface with strong polymer–filler interactions will decrease at a certain concentration. When the filler–filler interaction exceeds the polymer–filler interactions, the nanointerfacial areas for favorable stress transfer will decrease. The critical volume fraction for this decrease was estimated at 0.2 wt% C-rGONRs in the PVC nanocomposites based on the decreased toughness in uniaxial tension. At this critical concentration, the density started to decrease, supporting a strong correlation of nanoconfinement with the anomalous reinforcement in the PVC/C-rGONR nanocomposites.

Finally, the percolation model was fitted with the Young's modulus data as shown in Fig. 9. The shear modulus by percolation theory is calculated using eqn (3):[57]

$$G'_c = \frac{(1 - 2\Psi + \Psi X_r)G'_s G'_r + (1 - X_r)\Psi G'^2_r}{(1 - X_r)G'_r + (X_r - \Psi)G'_s} \quad (3)$$

where G' is the shear modulus, Ψ is the volume fraction of the percolating rigid phase, and X is the volume fraction. The subscripts s and r indicate soft phase and rigid phase, respectively.
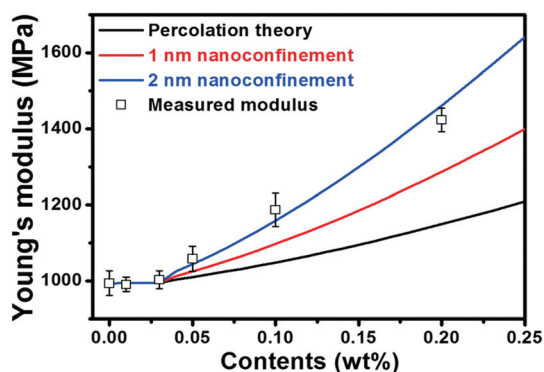

Fig. 9 Fitting percolation theory with the assumption of nanoconfined regions to the Young's modulus results.

Here, Ψ is calculated using the equation,

$$\Psi = 0, \quad X_r < X_c \quad (4)$$

$$\Psi = X_r \left(\frac{X_r - X_c}{1 - X_c}\right)^b, \quad X_r \geq X_c \quad (5)$$

where X_c is the critical volume fraction for percolation.

X_c is provided by the percolation threshold equation for the sheet-shaped filler:[58]

$$X_c = \frac{wtl}{\left(\frac{l}{3}\right)^3} \quad (6)$$

where w is the width, t is the thickness, and l is the length of the filler (eqn (4)–(6)). The calculated shear modulus was then converted to elastic Young's modulus using the Poisson's ratio information for PVC.

As shown in Fig. 9, a conventional percolation model could not fit the measured mechanical data. Instead, we assumed 1 nm and 2 nm of nanoconfined regions with the Young's modulus of the nanofiller. Nanoconfinement with a 1 nm thick interfacial area still could not explain the reinforcement effects of C-rGONRs. Remarkably, percolation theory assuming 2 nm nanoconfinement in the vicinity of nanofillers successfully fitted the measured mechanical properties. While this fitting is based on the nanoconfinement effects by pure topological constraints, it is known that the nanoconfinement is also strongly dependent on the polymer–filler interactions.[59] In general, the strongly attractive polymer–filler interactions generate larger nanoconfinement effects. Thus, estimation of the length scale for the nanoconfined interface was not for precise quantification. Similar nanoconfinement-induced thermomechanical reinforcement has previously been reported by dispersion of 2D nanosheets of transition metal dichalcogenides in poly(vinyl alcohol).[60] While the stiffness of the PVA nanocomposites increased at the sacrifice of elongational properties, we report a simultaneous increase in stiffness and strain-to-failure, indicating reinforcement in toughness/ energy-to-break. Along with the nanoconfinement-induced densification and thermomechanical reinforcement, this nanocomposite demonstrated dramatic enhancement in the oxygen barrier properties at an extremely low nanofiller content of 0.1 wt%.

Experimental

Preparation of C-rGONRs

GONRs were prepared according to a previously reported method.[27] Briefly, 150 mg of MWCNTs (95%, Hanwha Nanotech Inc., Korea) were immersed in concentrated sulfuric acid for 12 h at room temperature, and then 750 mg of KMnO$_4$ was added into the solution. The reaction mixture was stirred at room temperature for 1 h, and then heated to 55–70 °C for an additional 1 h. The reaction mixture was poured into 400 mL of ice containing 50 mL of 30% H$_2$O$_2$. The solution

was filtered using a polytetrafluoroethylene membrane and washed with distilled water several times. The as-prepared GONRs were dispersed in distilled water and frozen at −196 °C. The samples were then freeze-dried at −50 °C and 0.0045 mbar for 72 h. The resulting GONRs were dispersed in DMF (50 g) by ultrasonication and reacted with hydrazine (1 mL) at 90 °C for 2 h. After chemical reduction with hydrazine, C-rGONR dispersions (0.1 wt%) in DMF were obtained.[36]

Preparation of PVC/C-rGONR nanocomposites

3 g of PVC ($M_w \sim 43\,000$, $M_n \sim 22\,000$, Sigma-Aldrich) was dissolved in 30 g of the respective DMF solutions containing 0, 0.001, 0.003, 0.005, 0.01 or 0.02 wt% C-rGONRs to prepare PVC nanocomposites containing 0, 0.01, 0.03, 0.05, 0.1 or 0.2 wt% C-rGONRs, respectively at 60 °C and stirred for 30 min. Subsequently, the PVC and C-rGONR mixture solution was cast into a polytetrafluoroethylene dish and dried in a vacuum oven at 50 °C for 7 days to remove the residual solvent.

Characterization

The morphology of the samples was examined using FE-SEM (S-4300SE, Hitachi, Tokyo, Japan) and FE-TEM (JEM2100F, JEOL, Tokyo, Japan). The Raman spectra were recorded using a continuous-wave linearly polarized laser (wavelength: 514.5 nm; 2.41 eV; power: 16 mW). XRD (Rigaku, DMAX 2500) analysis was performed using Cu-Kα radiation (wavelength λ = 0.154 nm) with an instrument operated at 40 kV and 100 mA. The laser beam was focused *via* a 100× objective lens, resulting in a spot diameter of approximately 1 μm. The acquisition time was 10 s and three cycles were required to collect each spectrum. The chemical composition of the C-rGONRs was examined using XPS (PHI 5700 ESCA, Chanhassen, MN, USA) with monochromatic Al-Kα radiation ($h\nu$ = 1486.6 eV). Densities of the nanocomposites were obtained using a He pycnometer (Accupyc 1330, gas pycnometer, USA). Hg porosimetry is carried out using a Micromeritics Autopore IV 9500 at room temperature. IR spectra were recorded using a VERTEX 80v, Bruker Optics, Germany. DSC (PerkinElmer 7) tests were carried out in dry nitrogen gas at a flow rate of 10 mL min^{-1}. DSC calibration was conducted using indium as the standard, and the sample weight was 5.0 ± 0.1 mg. Tensile testing of the nanocomposites was performed using an Instron 4665 UTM in a uniaxial tension at 20 °C and 30% humidity. The dumbbell-shaped specimens were prepared in accordance with the ASTM D 638 standard for tensile testing. The cross-head speed was set to 2 mm min^{-1} for the dumbbell-shaped samples. The mean value of each product was determined as the average value of the five test specimens. The specific dispersion behaviors of C-rGONR in DMF were characterized using Turbiscan (Formulation, France) with a wavelength of 880 nm. OTR data were obtained with OX-TRAN Model 2/21 (MOCON, Minneapolis, MN, USA), by ASTM D3985 at 23 °C and 0% RH. The size of the tested sample was 50 cm^2.

Conclusions

In summary, chemically reduced graphene oxide nanoribbons (C-rGONRs) with multitudinous oxygen functional groups (C/O ratio of 6.3) were prepared by unzipping MWCNTs with a high contour length and persistence length. The one-dimensional morphological characteristics of C-rGONRs with numerous edge sites resulted in a high aspect ratio, a large surface area-to-volume ratio, and defective carbon structures. The inclusion of C-rGONRs in the PVC matrix induced a dramatic densification and T_g increase as well as reduced porosity and broadness of glass transition at a very low filler loading that cannot be explained by a simple rule of mixture, which is indicative of a nanoconfinement phenomenon at vicinal interfaces of nanofillers. At only 0.1 wt% of C-rGONR loading, the nanocomposite density increased by ∼0.032 g cm^{-3} with a 28.6 °C rise in T_g, suggesting significant manipulation of the segmental packing as well as free volume of the polymer matrices. Accordingly, the maximum oxygen barrier properties and mechanical toughness in tension were realized along with the greatest densification, which revealed a strong structure–property correlation in the nanocomposites. These anomalous nanoscale effects can be distinguished from the typical reinforcing behaviors directly originating from the physical properties of fillers. This study will provide a better understanding of design strategies for cost-effective functional polymer nanocomposites by minimizing the aggregation and concentration of expensive nanofillers.

Conflicts of interest

There are no conflicts to declare.

Acknowledgements

Notes and references

1 T. Keller, *Prog. Struct. Eng. Mater.*, 2001, **3**, 132–140.
2 C. Sanchez, B. Julian, B. Philippe and M. Popall, *J. Mater. Chem.*, 2005, **15**, 3559–3592.
3 P. J. Flory and J. Rehner, *Ann. N. Y. Acad. Sci.*, 1943, **44**, 419–429.
4 D. W. van Krevelen and K. te Nijenhuis, *Properties of polymers: their correlation with chemical structure; their numerical estimation and prediction from additive group contributions*, Elsevier Science, Amsterdam, Netherlands, 4th edn, 2009.
5 L. J. Fetters, D. J. Lohse, D. Richter, T. A. Witten and A. Zirkel, *Macromolecules*, 1994, **27**, 4639–4647.

6 M. F. Yu, O. Lourie, M. J. Dyer, K. Moloni, T. F. Kelly and R. S. Ruoff, *Science*, 2000, **287**, 637–640.

7 C. Lee, X. Wei, J. W. Kysar and J. Hone, *Science*, 2008, **321**, 385–388.

8 S. Stankovich, D. A. Dikin, G. H. B. Dommett, K. M. Kohlhaas, E. J. Zimney, D. A. Stach, R. D. Piner, S. T. Nguyen and R. S. Ruoff, *Nature*, 2006, **442**, 282–286.

9 C. Velasco-Santos, A. L. Martinez-Hernandez, F. T. Fisher, R. S. Ruoff and V. M. Castano, *Chem. Mater.*, 2003, **15**, 4470–4475.

10 M. A. Rafiee, J. Rafiee, Z. Wang, H. Song, Z. Z. Yu and N. Koratkar, *ACS Nano*, 2009, **3**, 3884–3890.

11 J. R. Potts, D. R. Dreyer, C. W. Bielawski and R. S. Ruoff, *Polymer*, 2011, **52**, 5–25.

12 Y. S. Yun, Y. H. Bae, D. H. Kim, J. Y. Lee, I. J. Chin and H.-J. Jin, *Carbon*, 2011, **49**, 3553–3559.

13 M. Y. Song, S. Y. Cho, N. R. Kim, S. H. Jung, J. K. Lee, Y. S. Yun and H.-J. Jin, *Carbon*, 2016, **108**, 274–282.

14 J. N. Coleman, M. Cadek, R. Blake, V. Nicolosi, K. P. Ryan, C. Belton, A. Fonseca, J. B. Nagy, Y. K. Gun'ko and W. J. Blau, *Adv. Funct. Mater.*, 2004, **14**, 791–798.

15 E. T. Thostenson, Z. Ren and T. W. Chou, *Compos. Sci. Technol.*, 2001, **61**, 1899–1912.

16 H. Kim, A. A. Abdala and C. W. Macosko, *Macromolecules*, 2010, **43**, 6515–6530.

17 Y. T. Liang and M. C. Hersam, *J. Am. Chem. Soc.*, 2010, **132**, 17661–17663.

18 S. Park and R. S. Ruoff, *Nat. Nanotechnol.*, 2010, **4**, 217–224.

19 A. A. Balandin, S. Ghosh, W. Bao, I. Calizo, D. Teweldebrhan, F. Miao and C. N. Lau, *Nano Lett.*, 2008, **8**, 902–907.

20 O. C. Compton, S. Kim, C. Pierre, J. M. Torkelson and S. T. Nguyen, *Adv. Mater.*, 2010, **22**, 4759–4763.

21 Y. H. Yang, L. Bolling, M. A. Priolo and J. C. Grunlan, *Adv. Mater.*, 2013, **25**, 503–508.

22 J. Z. Xu, T. Chen, C. L. Yang, Z. M. Li, Y. M. Mao, B. Q. Zeng and B. S. Hsiao, *Macromolecules*, 2010, **43**, 5000–5008.

23 M. Terrones, O. Martin, M. Gonzalez, J. Pozuelo, B. Serrano, J. C. Cabanelas, S. M. Vega-Diaz and J. Baselga, *Adv. Mater.*, 2011, **23**, 5302–5310.

24 J. Z. Xu, C. Chen, Y. Wang, H. Tang, Z. M. Li and B. S. Hsiao, *Macromolecules*, 2011, **44**, 2808–2818.

25 M. Rahmat and P. Hubert, *Compos. Sci. Technol.*, 2011, **72**, 72–84.

26 T. Kuilla, S. Bhadra, D. Yao, N. H. Kim, S. Bose and J. H. Lee, *Prog. Polym. Sci.*, 2010, **35**, 1350–1375.

27 D. V. Kosynkin, A. L. Higginbotham, A. Sinitskii, J. R. Lomeda, A. Dimiev, B. K. Price and J. M. Tour, *Nature*, 2009, **458**, 872–878.

28 T. H. Vo, M. Shekhirev, D. A. Kunkel, M. D. Morton, E. Berglund, L. Kong, P. M. Wilson, P. A. Dowben, A. Enders and A. Sinitskii, *Nat. Commun.*, 2014, **5**, 3189.

29 H. Zhao, K. Min and N. R. Aluru, *Nano Lett.*, 2009, **9**, 3012–3015.

30 A. A. Balandin, *Nat. Mater.*, 2011, **10**, 569–581.

31 M. Terrones, A. R. Botello-Mendez, J. Campos-Delgado, F. Lopez-Urias, Y. I. Vega-Cantu, F. Rodriguez-Macias, A. L. Elias, E. Munoz-Sandoval, A. G. Cano-Marquez, J. C. Charlier and H. Terrones, *Nano Today*, 2010, **5**, 351–372.

32 D. B. Shinde, J. Debgupta, A. Kushwaha, M. Aslam and V. K. Pillai, *J. Am. Chem. Soc.*, 2011, **133**, 4168–4171.

33 L. R. Radovic and B. Bockrath, *J. Am. Chem. Soc.*, 2005, **127**, 5917–5927.

34 T. Luo and J. R. Lloyd, *Adv. Funct. Mater.*, 2012, **22**, 2495–2502.

35 C. Gomez-Navarro, M. Burghard and K. Kern, *Nano Lett.*, 2008, **8**, 2045–2049.

36 A. Higginbotham, D. V. Kosynkin, A. Sinitskii, Z. Sun and J. M. Tour, *ACS Nano*, 2010, **4**, 2059–2069.

37 J. M. Mohr and D. R. Paul, *J. Appl. Polym. Sci.*, 1991, **72**, 1711–1720.

38 H. S. Lee, C. H. Yun, H. M. Kim and J. C. Lee, *J. Phys. Chem. C*, 2007, **111**, 18882–18887.

39 Y. S. Yun, G. Yoon, K. Kang and H.-J. Jin, *Carbon*, 2014, **80**, 246–254.

40 L. G. Cancado, K. Takai and T. Enoki, *Appl. Phys. Lett.*, 2006, **88**, 163106.

41 M. Y. Song, Y. S. Yun, N. R. Kim and H.-J. Jin, *RSC Adv.*, 2016, **6**, 19389.

42 M. Doxastakis, Y. L. Chen and J. J. de Pablo, *J. Chem. Phys.*, 2005, **123**, 034901.

43 A. Tuteja, P. M. Duxbury and M. E. Mackay, *Phys. Rev. Lett.*, 2008, **100**, 77801.

44 F. W. Starr, T. B. Schroder and S. C. Glotzer, *Macromolecules*, 2002, **35**, 4481–4492.

45 Y. Huang, X. Wang and D. R. Paul, *J. Membr. Sci.*, 2006, **277**, 219–229.

46 J. F. J. Coelho, P. M. F. O. Goncalves, D. Miranda and M. H. Gil, *Eur. Polym. J.*, 2006, **42**, 751–763.

47 J. Bicerano, A. F. Burmester, P. T. Delassus and R. A. Wessling, *ACS Symp. Ser.*, 1990, **423**, 126–158.

48 H. J. Salavagione and G. Martínez, *Macromolecules*, 2011, **44**, 2685–2692.

49 H. J. Salavagione, G. Ellis and G. Martínez, *J. Phys. Chem. C*, 2012, **116**, 18256–18262.

50 N. K. Lape, E. E. Nuxoll and E. L. Cussler, *J. Membr. Sci.*, 2004, **236**, 29–37.

51 H. Oh and P. F. Green, *Nat. Mater.*, 2009, **8**, 139.

52 S. K. Kim, N. A. Nguyen, J. J. Wie and H. S. Park, *Nanoscale*, 2015, **7**, 8864.

53 S. Vadukumpully, J. Paul, N. Mahanta and S. Valiyaveettil, *Carbon*, 2011, **49**, 198–205.

54 H. Wang, G. Xie, M. Fang, Z. Ying, Y. Tong and Y. Zeng, *Composites, Part B*, 2017, **113**, 278–284.

55 H. Wang, G. Xie, Z. Ying, Y. Tong and Y. Zeng, *J. Mater. Sci. Technol.*, 2015, **31**, 340–344.

56 H. Wang, G. Xie, C. Yang, Y. Zheng, Z. Ying, W. Ren and Y. Zeng, *Polym. Compos.*, 2017, **38**, 138–146.

57 M. M. Ruiz, J. Y. Cavaille, A. Dufresne, J. F. Gerard and C. Graillat, *Compos. Interfaces*, 2000, **7**, 117–131.

58 J. Li, P. C. Ma, W. C. Chow, C. K. To, B. Z. Tang and J. K. Kim, *Adv. Funct. Mater.*, 2007, **17**, 3207–3215.

59 A. Karatrantos, R. J. Composto, K. I. Winey and N. Clarke, *Macromolecules*, 2011, **44**, 9830–9838.

60 S. K. Kim, J. J. Wie, Q. Mahmood and H. S. Park, *Nanoscale*, 2014, **6**, 7430.